Coupled effects of electronic and nuclear energy deposition in UO 2 crystals: a high-resolution XRD study carried out at the MARS beamline of the SOLEIL synchrotron facility

Gaëlle Gutierrez, Alexandre Boulle, Denis Menut, Arthur Georgesco, Claire Onofri, Jean-Luc Béchade, Aurélien Debelle

Coupled effects of electronic and nuclear energy deposition in UO_2 crystals: a high-resolution XRD study carried out at the MARS beamline of the SOLEIL synchrotron facility

Gaëlle Gutierrez[a*], Alexandre Boulle[b], Denis Menut[c], Arthur Georgesco[a], Claire Onofri[d], Jean-Luc Béchade[a], Aurélien Debelle[e]

a. Université Paris-Saclay, CEA, Service de recherche en Corrosion et Comportement des Matériaux, SRMP, 91191 Gif Sur Yvette, France.

b. IRCER, CNRS UMR 7315, Centre Européen de la Céramique, 12 rue Atlantis, 87068 Limoges Cedex, France

c. Synchrotron SOLEIL, L'Orme des Merisiers, Saint Aubin BP48, Gif-sur-Yvette Cedex F-91192, France

d. CEA, DES, IRESNE, DEC, Cadarache, F-13108 St Paul lez Durance, France.

e. Université Paris-Saclay, CNRS/IN2P3, IJCLab, 91405 Orsay, France.

ABSTRACT

For the first time at the SOLEIL synchrotron facility's MARS beamline, UO_2 single-crystal-like samples underwent characterization, and strain depth profiles were established. Single crystals oriented along (110) and (111) were submitted to ion irradiation in the nuclear energy-loss regime (S_n) using 900 keV I^{2+} ions, and also with concomitant electronic energy deposition (S_e) using 27 MeV Fe^{9+} ions. X-ray diffraction measurements were conducted at the MARS beamline, specialized for radioactive material analysis. High-angular-resolution reciprocal space maps around asymmetrical reflections and conventional symmetrical θ/2θ scans were recorded. Analysis with the RaDMaX software allowed retrieving the strain depth profiles. Results reveal that the S_n-irradiated surface layer exhibits tensile strain along its normal with no in-plane strain, that this normal strain is partially relaxed by S_e. Both crystal orientations display similar behavior, but not with the same magnitude. Comparison with polycrystals indicates a more pronounced strain relaxation in the latter case.

Keywords: irradiation; nuclear fuel; X-ray diffraction; synchrotron; strain

Corresponding author: gaelle.gutierrez@cea.fraurelien.debelle@ijclab.in2p3.fr

I. Introduction

In a nuclear reactor, materials are inherently submitted to energetic particle irradiation, which includes neutron, fission fragments, alpha particles, and recoil atoms. During this process, the energetic particles interact with solids, thereby progressively losing their energy according to two distinct processes that depend on their velocity. These processes are described in details in several books (see [1, 2] for instance), and we thus only recall hereafter their characteristics relevant for this work. A projectile with a low velocity (as compared to the velocity of its own electrons) essentially interacts with condensed matter through elastic - also called nuclear or ballistic - collisions with the nuclei of the target atoms. If the transferred energy is greater than a threshold displacement energy (E_d), the knock-on atom is ejected from its lattice site, potentially inducing a collision cascade [2, 3]. The associated slowing-down process is described by the nuclear stopping power (S_n); hence, S_n hereafter denotes the ballistic collision regime. Swift ions essentially interact with electrons of the target atoms, inducing excitation and ionization events, and this slowing-down is described by the electronic stopping power (S_e); hereafter, we use S_e to refer to the ionization regime. A significant amount of this electronic energy can be transferred to the atomic network through an electron-phonon coupling, which may produce atomic displacements, but those latter do not necessarily add up to the ballistic defects. Indeed, synergistic effects, where both S_n and S_e are involved (either subsequently or simultaneously), rarely are the simple result of the algebraic sum of the two contributions when it comes to lattice disorder. The material can hence be driven to different microstructural states spanning from less to more disordered ones, depending on the considered material (see [2, 4-6] as a few examples of these coupled S_n-S_e effects). In any case, the material microstructure is significantly modified (as compared to an irradiation with a sole S_n beam), and the intensity of this change depends on the disorder level and type present when the S_n and S_e coupling takes place and on the magnitude of the S_e component [2, 4, 7]. Therefore, getting a better knowledge of the effects on the microstructure of the energy partitioning between the electronic and atomic networks constitutes an important issue to

address. Besides, coupling the two energy deposition processes presents the advantage of better reproducing actual in-service conditions, particularly regarding the nuclear fuel.

Uranium dioxide (UO_2) is the base compound of the most used nuclear fuel worldwide. It has consequently been the focus of a huge amount of both experimental and computational studies dealing with radiation effects. It is not in the scope of this paper to present a review of those effects; the reader can refer to [8] and references therein for this purpose. We simply want to recall here that regarding coupled S_n-S_e effects, only a few works have been carried out in UO_2, and the vast majority of them are experimental ones [9-14]. The major result recently reported is that the kinetics of the defect transformation sequence (*i.e.*, point defects, dislocation loops and finally, dislocation lines, as described in the above-mentioned papers) is drastically modified by an electronic energy deposition. The magnitude of this change depends on the current disorder level, on the amount of deposited energy and on the temporality of the deposition, *i.e.*, subsequent to S_n irradiation (S_n+S_e) or concomitant to S_n (S_n&S_e) [9, 14]. Indeed, sequential irradiation experiments (S_n+S_e) were conducted on polycrystals. A growth of dislocation loops was observed, but to a lesser extent than with simultaneous dual-beam irradiations. This result was evidenced in irradiated UO_2 pellets and put forward using several characterization techniques such as Raman spectroscopy, transmission electron microscopy (TEM) and/or X-ray diffraction (XRD). Regarding this latter technique, the first work clearly showing coupled S_n&S_e effects was carried out using a laboratory XRD device and focused on determining the strain/stress state of irradiated polycrystalline samples using an approach known as the $\sin^2\Psi$-method [15, 16]. It was demonstrated that the strain/stress level in the surface region (that is affected by the energetic ions) of S_n&S_e-irradiated pellets was significantly different from the one determined after the sole S_n irradiation [12]. Yet, the methodology used in [12] relies on some limiting assumptions inherent to the method itself and to the polycrystalline nature of the samples (see [17] for a review of the different approaches of the $\sin^2\Psi$ method). First, the sample being of polycrystalline nature, no information regarding a potential effect of the crystallographic orientation could be determined, although it is not absurd to envision that different orientations, i.e., exhibiting different elastic con-

stants, would exhibit different behavior regarding strain/stress development. Second, no strain/stress depth profile could be obtained (the information was averaged over the X-ray probed thickness), but it is highly expected that, with the used irradiation conditions, a flat strain profile would not develop, as already broadly reported in the literature [18].

In the current work, to go further into the understanding of this S_n&S_e synergistic effect, and to provide additional information about it, we continued the study on UO_2 irradiated in either the S_n or in the coupled S_n&S_e regimes, but with three major differences in the approach: (i) we investigated single-crystal-like samples (see section II for the meaning of this term) to limit the effects of elastic anisotropy (due to random crystalline orientation inherent in polycrystals) on the development of strain and the associated defect evolution, we examined both (110)- and (111)-oriented crystals to put forward any crystallographic direction influence on the synergy effect, and (ii) we performed high-resolution XRD measurements (at the MARS beamline), coupled with XRD signal refinement, to establish the strain/stress depth profiles.

II. Experimental details

II.1. UO_2 samples

(110)- and (111)-oriented UO_2 (0.3% ^{235}U) samples, coming from the Joint Research Center (JRC-K) in Ispra (Italy), were used in this study. These crystals are called “single-crystal-like” because they are high quality multi-crystals, as explained in [19] and further justified in this paper. Briefly, those samples are composed of a 2 to 3 very large (*i.e.*, mm size) crystals, exhibiting the same (hkl) orientation with respect to the sample surface, with slight angular misorientations with respect to each other (typically lower than 1 degree). These crystals were slice-shaped, then mechanically polished until mirror-like finish with diamond pastes down to 0.5 µm, and finally annealed at 1700 °C to remove any damage created during the polishing process, in a mixture of H_2/Ar gases containing 5 vol. % of H_2 to assure the stoichiometric ratio of O/U = 2. The lattice parameter of pristine samples was measured by XRD, as for irradiated samples (see Section II.2.), and found to be 0.5472 nm [19].

II.2. Irradiation conditions

Ion irradiations were carried out at the JANNuS-Saclay facility [20]. Two different ions were used, separately and simultaneously: 900 keV I^{2+} ions (to a fluence of $5.5x10^{14}$ cm^{-2}) for the S_n regime and 27 MeV Fe^{9+} ions (to a fluence of $1.1x10^{15}$ cm^{-2}) for the S_e regime. The flux of the I^{2+} ion beam was $4x10^{10}$ $cm^2.s^{-1}$, and that of the Fe^{9+} ion beam was 2 times higher to maximize the S_n&S_e synergy effect. It was taken care that no macroscopic increase in temperature above 25 °C occurred during these irradiations (as controlled by thermocouples). Using the commonly admitted threshold displacement energies of 20 and 40 eV for the O and U sub-lattices, respectively [21], the disorder induced by I^{2+} ion irradiation peaked, for a $5.5x10^{14}$ cm^{-2} fluence, at 4 dpa, and at 1.6 dpa for a $1.1x10^{15}$ cm^{-2} Fe^{9+} fluence (with a U:O ratio of 2 for both). The energy-loss deposition profiles, which are of primary interest in this work as our main purpose is to show a synergy between the energy deposition processes, are presented in Section III.1.

II.3. XRD measurements

High-resolution X-ray diffraction (HR-XRD) measurements were carried out at the MARS (Multi Analysis of Radioactive Samples) beamline of the SOLEIL synchrotron facility, dedicated to radioactive material analyses [22, 23]. As this is the first time that the results of such measurements on this beamline are reported in the literature, we provide in the Appendix substantial details about the setup and the procedure that we used. In the current Section, we present only the major information. The X-ray wavelength λ was set to 0.1537591 nm (see supplementary material). A point scintillation detector located behind a Ge(111) analyzer crystal mounted on the 2θ arm was used to record the diffracted x-rays. Specifically, reciprocal space maps (RSMs) were recorded in the vicinity of 424 and 006 reflections of the (110)- and (111)-oriented UO_2 crystals, respectively, with a step size of 0.008 ° for both ω and 2θ scanning motors (see appendix). In addition, conventional θ-2θ 1D scans were acquired around the 220 and 222 reflections, for each of the two crystal sets, respectively, using a 0.002 ° step size. The RSMs are plotted hereafter in (Q_x, Q_z) frames where Q_x and Q_z are, respectively, the in-plane and out-of-plane coordinates of the scattering vector **Q** (of amplitude $Q = 4\pi \sin\theta/\lambda$, θ being half the scattering angle); specifically, $Q_x = Q \sin(\omega - \theta)$ and $Q_x = Q \cos(\omega - \theta)$, where ω is the incidence

angle of the X-ray beam on the lattice planes parallel to the surface. The symmetric 1D scans are plotted as a function of the opposite the strain $-\varepsilon_{[hkl]} = -(d - d_B) / d_B \approx (Q - Q_B)/Q_B$ where d_B is the lattice spacing corresponding the Bragg peak with position Q_B, and $\varepsilon_{[hkl]}$ is the strain along the [hkl] direction (that is perpendicular to the crystal surface in the present case). These 1D XRD scans were simulated with the RaDMaX software [24] to extract the strain depth profiles in the irradiated region.

III. Results

III.1. Irradiation-induced energy-loss depth profiles

The S_n and S_e depth profiles were calculated, using the Iradina code [25], and are plotted in Fig.1. Those profiles are the object of a dedicated section because they allow to clearly explain which part of the bulk samples must be considered for each irradiation sequence. The maximum of S_n(I) reaches 4 keV/nm at ~80 nm, a value which is sufficient to induce in UO_2, *via* collision cascades, significant damage in the form of defect clusters. S_e(I) does not exceed 3 keV/nm, a low value that is admitted to only slightly affect the microstructure in UO_2. Moreover, this component is always present (*i.e.*, for both S_n and S_n&S_e irradiations), so that its potential effect on the disorder level is included in all experiments and it will thus not hamper the monitoring of the expected effect of S_e(Fe). Regarding this latter component, it is almost constant over the entire I^{2+} ion range, where it reaches 12 keV/nm, a value that has been shown to be sufficiently high to induce a change in the defect distribution created by elastic collisions in UO_2 polycrystalline pellets [9, 12, 14, 26]. S_n(Fe) is lower than 0.1 keV/nm over the entire I^{2+} ion range; this value increases to 0.8 keV/nm in the end-of-range of the Fe^{9+} ions. In both regions, this energy deposition can lead to defect creation; this latter point will be discussed hereafter.

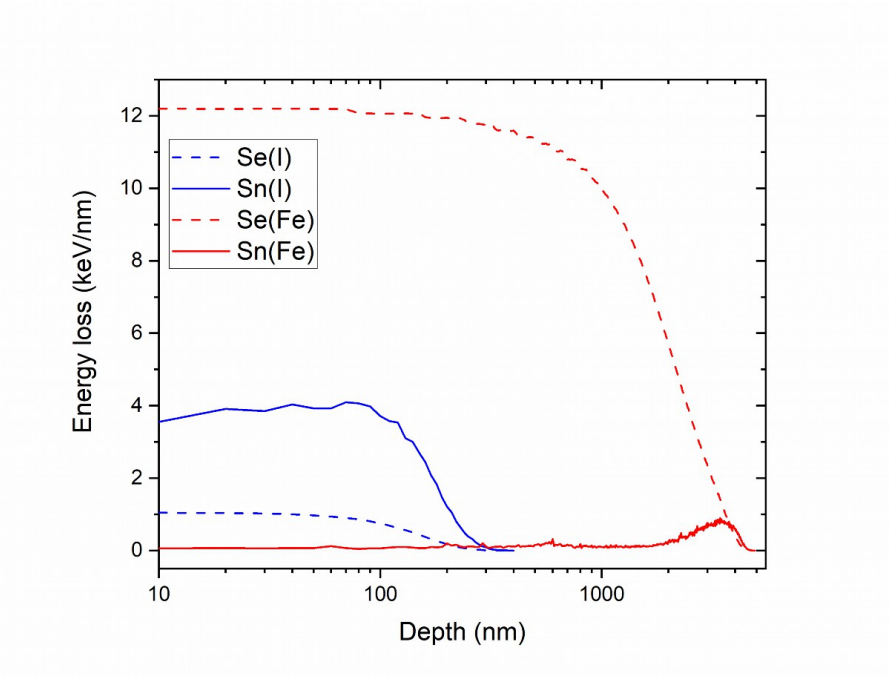

Fig. 1: Nuclear (S_n, solid lines) and electronic (S_e, dashed lines) energy-loss depth distributions of 900 keV I^{2+} and 27 MeV Fe^{9+} projectiles, as calculated using the Iradina code [25]; depth is in logarithmic scale.

III.2. Strain state of irradiated crystals

Fig.2 presents reciprocal space maps recorded in the vicinity of the 424 reflection of two (110)-oriented UO_2 crystals: the sample irradiated in the sole S_n regime (Fig.2a) and the one submitted to the coupled S_n&S_e regimes (Fig.2b). It is worth noting that this reflection (with hkl different from the crystal orientation) is sensitive to the presence of strain in the direction normal to the sample surface, so that, if such strains develop in the material they would be immediately detected in the data (see below). Such reflection is commonly referred to as an "asymmetric" reflection. A few characteristic features in the maps are important to mention; note that those features were also present on the maps (not shown here) recorded for the (111) crystallographic orientation. First, in Fig.2a (S_n regime), a high-intensity signal is recorded at coordinates Q_x = -48.714(5) nm^{-1} and Q_z = 48.715(5) nm^{-1} which correspond to those of the 424 reflection with the lattice parameter of pristine UO2 crystals (the digit in brackets corresponds to uncertainty). This signal hence arises from the unirradiated part of the samples that is probed by the X-rays. The additional streak that spreads, with continuous oscillations, towards low Q_z values is due to the irradiated layer; it signs the presence of a tensile strain profile

along the surface normal of the samples [27-29] which will be retrieved by simulating the 1D symmetric line scans presented in Section III.3 Fig.3. This signal is confined in a very narrow Q_x region (see red-yellow color in Fig.2a), with a low intensity diffuse scattering signal spreading along the Q_x direction (light blue color); both features indicate the presence of small defect clusters, like small dislocation loops, as previously observed in polycrystalline UO_2 irradiated in very similar irradiation conditions [9, 26]. Second, these features seem to be duplicated, yet with a much lower intensity, on the right-hand side of the map; this double signal comes from the presence of two large crystals, slightly misoriented one from the other, because, as mentioned in Section II, the crystals we used are in fact multi-crystals, or single-crystal-like crystals. It is worth emphasizing that this characteristic does not hamper the analysis of the XRD signal, as already demonstrated in [19, 30].

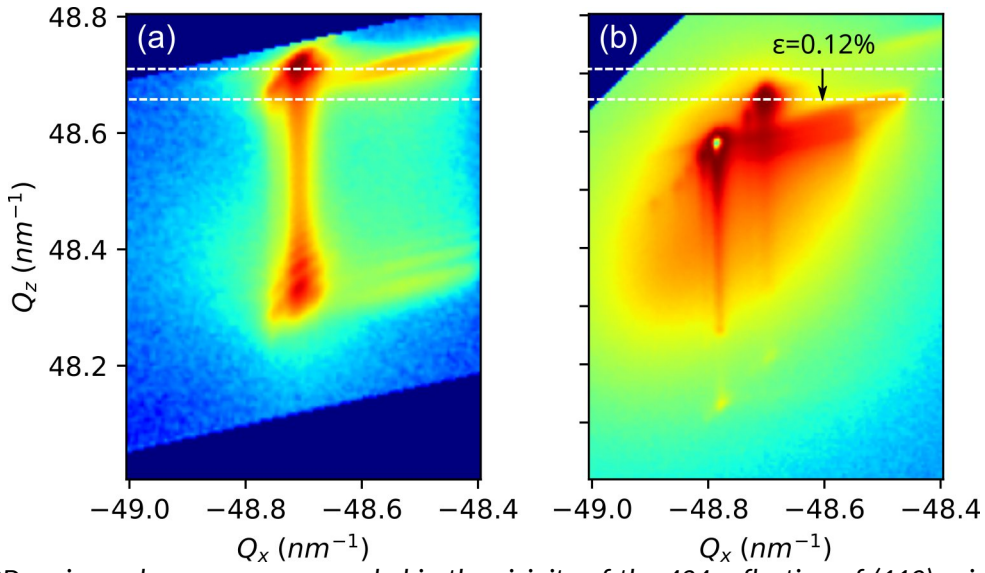

Fig. 2: XRD reciprocal space maps recorded in the vicinity of the 424 reflection of (110)-oriented UO_2 single crystals irradiated in the S_n regime (a) and in the coupled S_n&S_e regime (b). Intensity is plotted in log-scale with the common rainbow color-code (low to high intensity from blue to red).

The overall description of the RSM of Fig.2a (for the S_n-irradiated crystal) holds for the RSM of Fig.2b, *i.e.*, for the S_n&S_e-irradiated sample. Few differences can yet be noticed. First, though this has no consequences on the following, more mosaic blocks (i.e., more intense peaks) can be detected in the data. Second, the Q_z-coordinate of the peak in the high Q_z region differs from the one measured

for the S_n case, 48.655 vs 48.714 nm^{-1}. This difference (of ~0.12 % as depicted in Fig. 2b) can be explained by the fact that with an incidence angle around 12 °, the unirradiated part of the samples is not probed by the X-rays for the dual-beam irradiated crystals. Indeed, 99 % of the X-ray beam is absorbed within a thickness not larger than 3 µm as calculated with the methodology presented in [31], a thickness that is shallower than the Fe^{9+} ions end-of-range region. Hence, a large part of the Fe^{9+} ion path is sampled (see Fig. 1). The corresponding high-intensity signal arises at a lower Q_z-value as compared to that recorded for the pristine part of the S_n-irradiated sample (see white dashed lines in Fig.2), indicating that this region is experiencing a tensile strain along the surface normal. As it will be shown hereafter, this region corresponds to part of the S_n(Fe) profile along which the formation of defects has occurred (see Fig. 1). Third, and more important is the fact that the signal arising from the surface layer (affected by both S_n and S_e) spreads much less towards low Q_z values (as compared to the sole I^{2+} ion irradiation); in addition, it is also less confined in the Q_x region, meaning that the diffuse scattering component is more intense. These two characteristics constitute an evidence of a change in the spectrum (nature and/or density) of the S_n-induced defects, and most likely indicates a transformation from small dislocation loops to extended dislocation lines producing significant lattice disorder. Indeed, these latter does not induce a lattice swelling (hence, the strain decreases [32]), but they do induce a significant diffuse scattering [30]. This modification in the defect spectrum was put forward in polycrystalline UO_2 samples [9, 13, 26] with a combination of XRD measurements and TEM imaging; the current HR-XRD data suggest that this phenomenon also takes place in single-crystal-like UO_2. To finish with the RSMs, the RSM of the asymmetric 424 reflection displayed in Fig. 2, have both an in-plane (Qx // [001]) and an out-of-plane (Qz // [110]) scattering vector component. As such, they are sensitive to strain developing both in the in-plane and out-of-plane direction. As already noticed above, the fact the RSM exhibit an intensity streak along the Qz direction indicates the presence of a strain variation in the direction normal to the surface. Conversely, the lack of Qx variation along this streak, i.e. the streak is perfectly vertical (including the pristine part of the crystal), demonstrates that both the pristine part and the irradiated region of the crystal share the same lattice parameter in the

direction perpendicular to the surface normal, and that no in-plane strain variations occur in the irradiated region.

This strain state can be explained considering that the thick, rigid part of the unirradiated sample constrains the irradiated layer to keep its lateral dimension upon irradiation-induced swelling, and hence, a biaxial, compressive in-plane stress ($\sigma_{xx}=\sigma_{yy}=\sigma_{//}$) develops to prevent the in-plane lattice parameter change, which gives rise to an additional out-of-plane strain via Poisson reaction (see Section III.4) [29]

An analogy with a thin film deposited on a substrate can be made considering this system made of a thin irradiated layer at the surface of a bulk sample. This analogy with an epitaxial layer deposited onto a substrate holds even when relaxation phenomena take place to relieve the stored elastic energy, and the layer simply recovers its stress-free, intrinsic lattice parameter. A major difference though is that strain relaxation in thin films can take place during growth, whereas no such mechanisms can, obviously, be activated in an irradiated crystal where no growth take place per se. Different mechanisms are therefore activated to relieve the strain energy associated to lattice swelling and such as the progressive evolution of the defect structure in the material.

A similar situation has been observed in other ceramic oxide materials relevant for a comparison with the current work, namely single-crystalline UO_2 [30], ZrO_2 [33] and MgO [34]. This strain state was, based on these previous results, assumed to hold in a former study of dual-beam S_n&S_e irradiation experiments of UO_2 without further proof [12]; we demonstrate below that it does hold for these specific irradiation conditions. This typical strain state is finally described by the strain and stress tensors given in Eq.1 (which is extensively described in [29]). It will be used in the following to compare the response of the UO_2 crystals to irradiation according to their crystallographic orientation.

$$\begin{pmatrix} 0 & 0 & 0 \\ 0 & 0 & 0 \\ 0 & 0 & \epsilon_{zz} \end{pmatrix} \begin{pmatrix} \sigma_{xx} & 0 & 0 \\ 0 & \sigma_{yy} & 0 \\ 0 & 0 & 0 \end{pmatrix} \quad \text{Eq. 1}$$

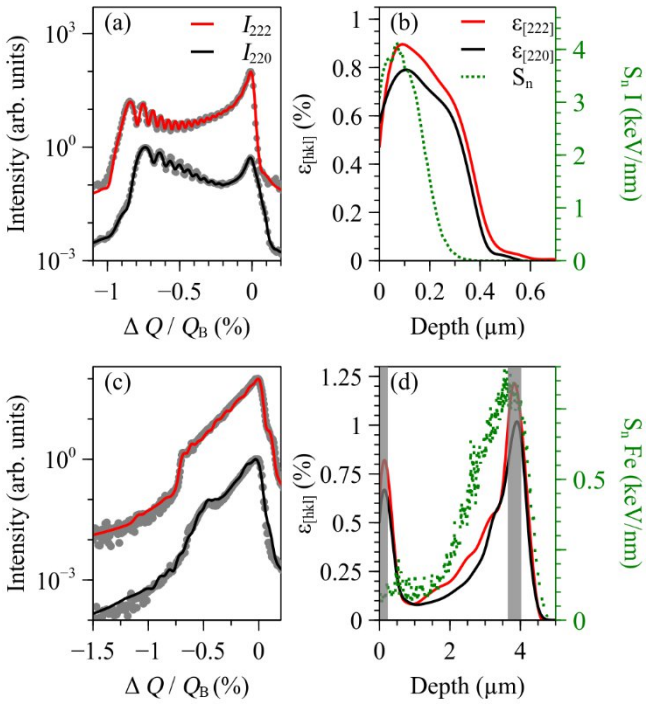

Fig.3: HR-XRD scans recorded around both the 220 and the 222 reflections of the (110)- and (111)-oriented UO_2 single crystals, respectively. Curves corresponding to samples irradiated in the S_n regime are displayed in (a), and those for the coupled S_n&S_e regimes are plotted in (c). The corresponding strain depth profiles, derived from the fitting of these curves, are presented in (b) and (d), respectively. In figures 3b and 3d are also provided the S_n(I) and the S_n(Fe) profiles, respectively, for the purpose of comparison with the strain depth profiles. The gray regions in (d) indicate the region of high disorder where the determined lattice strain is less reliable; therefore, strain values were taken right below this region.

III.3. Strain depth profiles of irradiated crystals

In Fig.3 are displayed symmetric 1D scans recorded around the 220 and 222 reflections of the (110)- and (111)-oriented irradiated UO_2 crystals, respectively. Given the strain state of the irradiated samples, these scans are equivalent to scans along the Q_z direction in the RSMs presented in Fig.2; however, they have been recorded in a symmetric geometry, with a higher angular resolution. These curves exhibit classical features of irradiated single-crystals (see [28, 29] and references therein), including UO_2 [19, 30]. First, an intense peak is visible on the right-hand side of the plots and more pre-

cisely at a zero-strain level ($\Delta Q/Q_B = \epsilon_{[hkl]} = 0$); this signal emanates from the unirradiated part of the samples and it is present for both orientations and for both irradiation conditions. Indeed, in contrast to the maps displayed in Fig.2 for which a relatively low incidence angle (max. ~12 °) was used, for the current symmetric reflections, the incidence angle is between ~23 and 30 °, which allows probing the crystal beyond the Fe^{9+} ion range. An additional signal spreading towards high $\Delta Q/Q_B$ values is measured, originating from the irradiated layers. As expected from the RSMs, this signal exhibits a fringe pattern, better defined and spreading towards lower Q_z values for S_n-irradiated samples than for S_n&S_e-irradiated ones. These differences are related, as above-explained, to a less disordered but more strained lattice for the former crystals than for the latter. The fitting of the experimental curves allowed determining the strain depth profile in each crystal set (Figs. 3b-d). This strain profile, for S_n-irradiated samples, looks similar to the S_n(I) depth distribution (plotted in green dotted line in Fig.3b), both in shape (peak-shape) and depth-location (maximum at ~80 nm), but it is broader than the S_n(I) depth profile. These findings are in line with previous studies of irradiated ceramic oxides that, as UO_2, do not undergo amorphization upon irradiation [30, 35]. For dual-beam irradiated samples, the strain profile appears to be more complicated: it exhibits a first peak at ~80 nm, followed by a weak gradual increase of strain over roughly 3 µm and it ends with a second peak located at ~3.6 µm. This gradual increase explains the shift in the coordinates of the main Bragg peak noted in the map of Fig.2b. The region below 80 nm, along with the deep peak, are due to the ballistically-induced disorder generated by the Fe^{9+} ions, the corresponding strain profile being indeed comparable to the S_n(Fe) profile. As above-mentioned, the nuclear energy-loss of the 27 MeV Fe^{9+} ions is sufficient to lead to the creation of defects in UO_2. More importantly, the shallow peak appears similar in shape and position to the one observed for the single-beam irradiation, but with an overall lower level (this observation is further discussed below). This strain reduction can hence be attributed to S_e(Fe), which agrees with the same finding derived from the RSMs of Fig.2. Previous studies in polycrystals put forward a similar partial strain relaxation occurring because of the formation of dislocation lines [26], that do not induce a lattice strain, at the expense of dislocation loops, that do generate a lattice swelling [36]. This

result holds for our model (single-crystal-like) UO_2 samples, and for the two different crystallographic orientations. It should be mentioned that in the highly strained regions (indicated by grey areas in Fig. 3d), the level of disorder is very high, with a static Debye-Waller reaching almost zero (curves not shown). This is a direct indication of a morphological change of the defect structure, although it may also indicate amorphization. However, based on previous studies [32, 37], the most likely scenario is that the defects, namely dislocation loops, inducing strain are replaced with defects dislocation lines inducing disorder, but no (elastic) strain. In these highly perturbed regions, and notably around 80 nm, the maximum strain cannot be reliably determined, as shown in [38-41] but, as mentioned above, it very likely drops to very low values. Moreover, the decrease in strain is readily visible, qualitatively, by a direct observation of the XRD curves (see Fig. 3c) where the strain-induced peak shifts towards lower strain values between the S_n and the S_n&S_e data. Furthermore, the position of the peaks in the XRD curves correspond the strain value measured just below the heavily damaged region, with maximum values of 0.7% and 0.58% for the (111) and (110) orientations respectively. Those values will therefore be used for the calculations below.

III.4. Comparison between (110) and (111) orientations

As above-mentioned, (110) and (111) orientations behave similarly upon S_n irradiation, and also upon S_n&S_e irradiations. Yet, a discrepancy seems to exist between these two orientations, as the maximum strain level (in the surface region, i.e., that affected by S_n deposition processes in both cases) is found to be lower for the former orientation than for the latter. But this discrepancy is only apparent and related to the material elastic properties. Indeed, one must note that the measured, total strain (ε^{tot}) is the sum of two contributions: one coming from the defects (ε^{def}) formed during the irradiation process, which is an isotropic lattice swelling, and one frequently referred to as the 'substrate reaction' (ε^{SR}). As mentioned earlier, this latter arises because, upon irradiation-induced swelling, as the irradiated layer is clamped on the unirradiated part of the crystal, hence preventing lateral expansion. Therefore, an in-plane compressive stress develops to cancel the in-plane dimensional change, which generates a Poisson effect in the perpendicular direction, *i.e.*, along the surface

normal direction that is probed during our XRD measurements. This description has been proposed decades ago in implanted materials [27] and was more recently applied to irradiated ceramic oxides [29, 30, 33]. As UO_2 is an elastically anisotropic material, the Poisson effect magnitude differs with the crystal orientation; hence, direct comparison of the measured strain can lead to misleading interpretations of the material response to irradiation (as shown in [30, 42]). Using equations (1a) and (1b) and the elastic constants, C_{ij}, for UO_2 given in [43] (assuming they do not change under irradiation, as it was shown in [44] that they do not evolve by more than 13 %), it is possible to extract, from the total strain (that do depends on the crystallographic direction) $e^{tot}_{[hkl]}$, the strain due to defects only, $e^{tot}_{[hkl]}$ (which is not affected by the Poisson effect). Note that, in order to consider only the S_n(I)-induced strain, the ~0.12 % strain level due to S_n(Fe), determined in the previous section, was subtracted for the S_n&S_e experiments. The strain values, estimated at the maximum of the shallow strain profile, are reported in Table I.

$$e^{def}_{[110]} = \frac{C_{11}+ C_{12}+ 2C_{44}}{2(C_{11}+ 2C_{12})} \times e^{tot}_{[110]} \quad 1(a)$$

$$e^{def}_{[111]} = \frac{C_{11}+2C_{12}+ 4C_{44}}{3(C_{11}+ 2C_{12})} \times e^{tot}_{[111]} \quad 1(b)$$

Considering first the maximum value of ϵ^{def} after the sole S_n irradiation, ϵ^{def}_{max}, it reaches ~0.4 %, for a dpa peaking at 4, in perfect agreement with the value reported in [30]. Above all, it appears that this value is the same (within the uncertainty of the values, estimated to 0.02 percentage point on the strain) for both orientations. This result indicates that the ballistic-defect distribution does not depend on the crystallographic orientation, which makes sense, as the defect production process related to the formation of collision cascades developing in the nuclear energy-loss regime is a stochastic process. A same conclusion was already put forward in similar, single, S_n irradiation experiments [30]; it is here confirmed. It is also, more importantly, demonstrated here that for dual-beam, S_n&S_e irradiations, $e^{def}_{[110]}$ is almost identical for both orientations. This finding suggests that the defects created by S_n(I) are affected, overall, in a similar way by S_e(Fe) for both orientations. Quantitatively, this outcome is demonstrated by a relative strain decrease (between S_n and S_n&S_e) of ~25 % and ~20 % for the (110)

and (111) orientations, respectively. Given the almost feature-less signal corresponding to the S_n&S_e-irradiated samples, this difference is most likely related to the limited accuracy in the fitting procedure. A more systematic study would be required to provide conclusive elements about this potential difference between the two orientations. It is also worth mentioning that in UO_2 polycrystals, this strain relaxation was found to reach a much higher level, ~70 % [26], yet in conditions less favorable than the current ones (because in [26] the S_n on S_e ion flux was lower than 1, while it is close to 2 in the current work). Therefore, although overall, 'single' and polycrystals seem to behave similarly, they exhibit some differences, their respective response to S_e being an important one. Such a difference between single and polycrystals has already been reported in the literature [45, 46], with a demonstrated effect of the grain size on the electronic energy dissipation as they can act like sinks favoring the defects diffusion at the interfaces (although in [45, 46], grains were much smaller than the micrometer-sized ones of our polycrystals). This body of evidence clearly put forward the necessity to conduct more systematic comparative studies between UO_2 single and polycrystal samples, for the twofold purposes of fundamental understanding of the coupled S_n&S_e effects on the UO_2 microstructure and practical knowledge of the actual fuel behavior in-pile.

Table I: Total (measured) strain determined from the fit, with the RaDMaX code [24], of the HR-XRD scans presented in Fig.3; the corresponding strain due to defects only (see text) is also provided. For the S_n case, the values are given at the maximum of the strain profiles. For the S_n&S_e case, the strain values correspond to the maximum value right below the heavily damaged region.

	ε_{max}^{tot} **(%)**		ε_{max}^{def} **(%)**	
	{110}-orientation	{111}-orientation	{110}-orientation	{111}-orientation
S_n	**0.78 ± 0.02**	**0.88 ± 0.02**	**0.39 ± 0.02**	**0.40 ± 0.02**
S_n&S_e	**0.58 ± 0.03**	**0.70 ± 0.03**	**0.29 ± 0.03**	**0.32 ± 0.03**

IV. Conclusion

Summarizing, both (110) and (111)-oriented UO_2 single-crystal-like were irradiated in either the sole S_n regime or in the coupled S_n&S_e regimes (*i.e.*, simultaneously with two ion beams). HR-XRD measurements were performed at the MARS beamline of the SOLEIL synchrotron facility to finely map the reciprocal space of those radioactive nuclear materials. These experimental data were fitted with the RaDMaX code. This dedicated methodology allowed reaching the following important conclusions:

- (i) Upon S_n irradiation, a tensile strain depth profile develops, with a strain confined along the surface normal of the samples (no in-plane strain was detected) within a thickness of ~0.5 µm.
- (ii) Upon S_n&S_e irradiation, within the first ~0.5 µm, a strain profile similar to the previous one is observed, albeit with a reduced level, because the deposited electronic energy (S_e) modifies the defect distribution induced by S_n; the total strain profile extends towards much greater depth (~ 5 µm) because of the larger Fe^{9+} ion range.
- (iii) Both (i) and (ii) hold for the two crystallographic orientations investigated. Moreover, the contribution of defects to the overall strain was found to be identical for both orientations, demonstrating that strain build-up is independent on the crystallographic orientation.
- (iv) Finally, it was found that the S_e-induced strain relaxation was slightly more pronounced for the {110} orientation, although it could not be firmly concluded whether this difference is the manifestation of an actual anisotropy in the strain relaxation, or if it is induced by the reduced accuracy of the data fitting procedure in the case of large, damaged depths. More systematic studies are required to provide conclusive data about this latter aspect.

These results should provide new insights on the understanding of the in-pile behavior of the nuclear fuel. Ultimately, a comprehensive description and understanding of these complex phenomena of S_n

and S_e coupling should provide useful material knowledge for the design of advanced fuels with a prolonged lifetime.

Acknowledgements

Authors would like to thank the JANNuS-Saclay facility staff for their help during the ion irradiations. They also acknowledge Prof. F. Garrido and the radiation protection staff of IJCLab, as well as the SOLEIL radiation protection people, for handling the back and forth UO_2 sample transport between the two places.

Data availability statement

The raw/processed data presented in this work will be shared upon request.

Apprendix: technical details about the HR-XRD end-station of the MARS beamline of the SOLEIL synchrotron

The MARS beamline is dedicated to the investigation in the hard X-ray range of radioactive, essentially nuclear, materials [22, 23]. The beamline optics consists of a water-cooled double-crystal monochromator, which is used to select the incident energy of the X-ray beam and for horizontal focalization, and of two large water-cooled reflecting mirrors that are used for high-energy rejection and vertical collimation. In the current work, the monochromator was a set of Si(111) crystals and the mirrors were a set of Si strips. The vertical x horizontal FWHM dimensions of the beam size were about 150 x 300 m^2; the beam divergence in vertical and horizontal directions amounted to 0.01° and 0.06°, respectively. The incident energy was calibrated using the absorption K-edge of a nickel metallic foil (8.333 keV). The HR-XRD end-station is equipped with a four-circle diffractometer that was used in reflection mode with a horizontal sample surface, thus the scattering plane is vertical. Samples were doubly confined in two airtight nested sample holders, the first one in the form of a 13-µm thick Kapton foil and the second one being a commercial (Bruker) PEEK dome. Two types of detectors were used for this study: (i) a MerlinX Medipix3 single chip 256 x 256 pixels sizing 55 x 55 μm^2 (from Quantum detectors, UK), which is a hybrid photon counting detector; (ii) a set of 24 point scintillation detectors located behind a set of Ge(111) analyzer crystals mounted on the 2θ arm. The instrumental resolution function was estimated through the diffraction pattern measurement of the LaB_6 660b NIST powder and the diffraction peak FWHM was close to 0.013°. Thus, after correction of the end-station geometry, it was found that the wavelength λ was equal to 0.1537591 nm.

The MerlinX detector was used to rapidly align the samples (whose surface normal is usually a few degrees off the crystallographic planes normal) and to record 3D reciprocal space maps (RSMs); in the current paper, those 3D maps are not presented. The point detectors were used to collect High Resolution 2D RSMs and 1D line scans; these data are reported here. Specifically, RSMs were recorded in the vicinity of the (asymmetric) 442 and 006 reflection of {110}- and {111}-oriented UO_2 crystals, respectively, with a step size of 0.008 °; in addition, symmetric 1D scans were collected around the 220 and 222 reflections, for each of the two crystal sets, respectively, using a 0.002 ° step size. The

RSMs are plotted in (Q_x, Q_z) frames where Q_x and Q_z are, respectively, the in-plane and out-of-plane coordinates of the scattering vector **Q** (of amplitude $Q = 4\pi sin\theta/$, θ being half the scattering angle); specifically, $Q_x = Qsin(\omega - \theta)$ and $Q_z = Qcos(\omega - \theta)$, where ω is the incidence angle of the X-ray beam on the lattice planes parallel to the surface. The symmetric 1D scans are plotted as a function of $(Q - Q_B)/Q_B = (Q)/Q_B = -\varepsilon_{[hkl]}$, with Q_B the scattering angle corresponding the Bragg peak, and $\varepsilon_{[hkl]}$ is the strain along the [hkl] direction (that is perpendicular to the crystal surface in the present case). These 1D XRD scans were simulated with the RaDMaX software [24] in order to extract the strain depth profiles in the irradiated region.

References

[1] M. Nastasi, J. Mayer, J.K. Hirvonen, Ion-Solid Interactions: Fundamentals and Applications, Cambridge University Press, Cambridge, 1996.
[2] W.E. Wesch W., Ion Beam Modification of Solids: Ion-Solid Interaction and Radiation Damage, Springer Series in Surface Sciences, 61 (2016).
[3] R.S. Averback, T.D. De La Rubia, Displacement Damage in Irradiated Metals and Semiconductors, in: H. Ehrenreich, F. Spaepen (Eds.) Solid State Physics, Academic Press, 1998, pp. 281-402.
[4] Y. Zhang, W.J. Weber, Ion irradiation and modification: The role of coupled electronic and nuclear energy dissipation and subsequent nonequilibrium processes in materials, Applied Physics Reviews 7(2020) 041307.
[5] A. Chakravorty, B. Singh, H. Jatav, S. Ojha, J. Singh, D. Kanjilal, D. Kabiraj, Intense ionizing irradiation-induced atomic movement toward recrystallization in 4H-SiC, Journal of Applied Physics, 128 (2020).
[6] D. Iancu, E. Zarkadoula, M.D. Mihai, C. Burducea, I. Burducea, M. Straticiuc, Y. Zhang, W.J. Weber, G. Velişa, Revealing two-stage phase transition process in defective KTaO3 under inelastic interactions, Scripta Materialia, 222 (2023) 115032.
[7] A. Debelle, L. Thomé, I. Monnet, F. Garrido, O.H. Pakarinen, W.J. Weber, Ionization-induced thermally activated defect-annealing process in SiC, Physical Review Materials, 3 (2019) 063609.
[8] T. Wiss, A. Benedetti, E. De Bona, 2.05 - Radiation Effects in UO2☆, in: R.J.M. Konings, R.E. Stoller (Eds.) Comprehensive Nuclear Materials (Second Edition), Elsevier, Oxford, 2020, pp. 125-148.
[9] G. Gutierrez, M. Bricout, F. Garrido, A. Debelle, L. Roux, C. Onofri, Irradiation-induced microstructural transformations in UO2 accelerated upon electronic energy deposition, Journal of the European Ceramic Society, (2022).
[10] B. Marchand, N. Moncoffre, Y. Pipon, N. Bérerd, C. Garnier, L. Raimbault, P. Sainsot, T. Epicier, C. Delafoy, M. Fraczkiewicz, C. Gaillard, N. Toulhoat, A. Perrat-Mabilon, C. Peaucelle, Xenon migration in UO2 under irradiation studied by SIMS profilometry, Journal of Nuclear Materials, 440 (2013) 562-567.
[11] N. Djourelov, B. Marchand, H. Marinov, N. Moncoffre, Y. Pipon, N. Bérerd, P. Nédélec, L. Raimbault, T. Epicier, Study of temperature and radiation induced microstructural changes in Xe-implanted UO2 by TEM, STEM, SIMS and positron spectroscopy, Journal of Nuclear Materials, 443 (2013) 562-569.
[12] G. Gutierrez, D. Gosset, M. Bricout, C. Onofri, A. Debelle, Effect of coupled electronic and nuclear energy deposition on strain and stress levels in UO2, Journal of Nuclear Materials, 519 (2019) 52-56.
[13] M. Bricout, G. Gutierrez, C. Baumier, C. Bachelet, D. Drouan, F. Garrido, C. Onofri, Synergy of electronic and nuclear energy depositions on the kinetics of extended defects formation in UO2, based on in situ TEM observations of ion-irradiation-induced microstructure evolution, Journal of Nuclear Materials, 554 (2021) 153088.
[14] G. Gutierrez, H. Guessous, D. Gosset, M. Bricout, I. Monnet, F. Garrido, C. Onofri, G. Adroit, A. Debelle, Defect evolution under intense electronic energy deposition in uranium dioxide, Journal of Nuclear Materials, 578 (2023) 154375.
[15] V. Hauk, Structural and residual stress analysis by nondestructive methods: Evaluation-Application-Assessment, (1997).
[16] I.C. Noyan, J.B. Cohen, Residual stress: measurement by diffraction and interpretation, Springer2013.
[17] U. Welzel, J. Ligot, P. Lamparter, A.C. Vermeulen, E.J. Mittemeijer, Stress analysis of polycrystalline thin films and surface regions by X-ray diffraction, Journal of Applied Crystallography, 38 (2005) 1-29.
[18] A. Boulle, A. Debelle, Strain-profile determination in ion-implanted single crystals using generalized simulated annealing, Journal of Applied Crystallography, 43 (2010) 1046-1052.
[19] A. Debelle, A. Boulle, F. Garrido, L. Thomé, Strain and stress build-up in He-implanted UO2 single crystals: an X-ray diffraction study, J. Mater. Sci., 46 (2011) 4683-4689.

[20] A. Gentils, C. Cabet, Investigating radiation damage in nuclear energy materials using JANNuS multiple ion beams, Nuclear Instruments and Methods in Physics Research Section B: Beam Interactions with Materials and Atoms, 447 (2019) 107-112.
[21] J. Soullard, High voltage electron microscope observations of UO2, Journal of Nuclear Materials, 135 (1985) 190-196.
[22] B. Sitaud, P.L. Solari, S. Schlutig, I. Llorens, H.J.J.o.n.m. Hermange, Characterization of radioactive materials using the MARS beamline at the synchrotron SOLEIL, 425 (2012) 238-243.
[23] I. Llorens, P.L. Solari, B. Sitaud, R. Bes, S. Cammelli, H. Hermange, G. Othmane, S. Safi, P. Moisy, S.J.R.A. Wahu, X-ray absorption spectroscopy investigations on radioactive matter using MARS beamline at SOLEIL synchrotron, 102 (2014) 957-972.
[24] A. Boulle, V. Mergnac, RaDMaX online: a web-based program for the determination of strain and damage profiles in irradiated crystals using X-ray diffraction, J. Appl. Cryst, 53 (2020) 587.
[25] J.-P. Crocombette, C. Van Wambeke, Quick calculation of damage for ion irradiation: implementation in Iradina and comparisons to SRIM, EPJ Nuclear Sciences Technologies, 5 (2019) 7.
[26] M. Bricout, C. Onofri, A. Debelle, Y. Pipon, R.C. Belin, F. Garrido, F. Leprêtre, G. Gutierrez, Radiation damage in uranium dioxide: Coupled effect between electronic and nuclear energy losses, Journal of Nuclear Materials, 531 (2020) 151967.
[27] S.I. Rao, C.R. Houska, Residual stress gradients along ion implanted zones - cubic crystals, J. Mater. Sci., 25 (1990) 2822-2826.
[28] A. Boulle, A. Debelle, Strain-profile determination in ion-implanted single crystals using generalized simulated annealing, J. Appl. Cryst, 43 (2010) 46.
[29] A. Debelle, A. Declémy, XRD investigation of the strain/stress state of ion-irradiated crystals, Nuclear Instruments and Methods in Physics Research Section B: Beam Interactions with Materials and Atoms, 268 (2010) 1460-1465.
[30] T.H. Nguyen, A. Debelle, A. Boulle, F. Garrido, L. Thomé, V. Demange, Mechanical response of UO2 single crystals submitted to low-energy ion irradiation, Journal of Nuclear Materials, 467 (2015) 505-511.
[31] D. Simeone, G. Baldinozzi, D. Gosset, S. Le Caer, J.-F. Bérar, Grazing incidence X-ray diffraction for the study of polycrystalline layers, Thin Solid Films, 530 (2013) 9-13.
[32] A. Debelle, J.-P. Crocombette, A. Boulle, E. Martinez, B.P. Uberuaga, D. Bachiller-Perea, Y. Haddad, F. Garrido, L. Thomé, M. Béhar, How relative defect migration energies drive contrasting temperature-dependent microstructural evolution in irradiated ceramics, Physical Review Materials, 2 (2018) 083605.
[33] A. Debelle, A. Boulle, F. Rakotovao, J. Moeyaert, C. Bachelet, F. Garrido, L. Thomé, Influence of elastic properties on the strain induced by ion irradiation in crystalline materials, Journal of Physics D: Applied Physics, 46 (2013) 045309.
[34] D. Bachiller-Perea, A. Debelle, L. Thomé, J.P. Crocombette, Study of the initial stages of defect generation in ion-irradiated MgO at elevated temperatures using high-resolution X-ray diffraction, J. Mater. Sci., 51 (2016) 1456-1462.
[35] A. Debelle, A. Declémy, L. Vincent, F. Garrido, L. Thomé, XRD contribution to the study of Cs-implanted cubic zirconia, Journal of Nuclear Materials, 396 (2010) 240-244.
[36] A. Debelle, J.-P. Crocombette, A. Boulle, A. Chartier, T. Jourdan, S. Pellegrino, D. Bachiller-Perea, D. Carpentier, J. Channagiri, T.H. Nguyen, F. Garrido, L. Thomé, Lattice strain in irradiated materials unveils a prevalent defect evolution mechanism, 2 (2018) 013604.
[37] A. Boulle, A. Chartier, A. Debelle, X. Jin, J.-P. Crocombette, Computational diffraction reveals long-range strains, distortions and disorder in molecular dynamics simulations of irradiated single crystals, Journal of Applied Crystallography, 55 (2022) 296-309.
[38] D.R. Pereira, S. Magalhães, C. Díaz-Guerra, M. Peres, J.G. Correia, J.G. Marques, A.G. Silva, E. Alves, S. Cardoso, P.P. Freitas, K. Lorenz, Estimating the uncertainties of strain and damage analysis by X-ray diffraction in ion implanted MoO3, Nuclear Instruments and Methods in Physics Research Section B: Beam Interactions with Materials and Atoms, 478 (2020) 290-296.

[39] A. Boulle, A. Debelle, J.B. Wallace, L.B. Bayu Aji, S.O. Kucheyev, The amorphization of 3C-SiC irradiated at moderately elevated temperatures as revealed by X-ray diffraction, Acta Materialia, 140 (2017) 250-257.
[40] A. Debelle, J. Channagiri, L. Thomé, B. Décamps, A. Boulle, S. Moll, F. Garrido, M. Behar, J. Jagielski, Comprehensive study of the effect of the irradiation temperature on the behavior of cubic zirconia, Journal of Applied Physics, 115 (2014).
[41] J. Channagiri, A. Boulle, A. Debelle, Determination of strain and damage profiles in irradiated materials: Application to cubic zirconia irradiated at high temperature, Nuclear Instruments and Methods in Physics Research Section B: Beam Interactions with Materials and Atoms, 327 (2014) 9-14
[42] A. Richard, E. Castelier, H. Palancher, J.S. Micha, H. Rouquette, A. Ambard, P. Garcia, P. Goudeau, Multi-scale X-ray diffraction study of strains induced by He implantation in UO2 polycrystals, Nuclear Instruments and Methods in Physics Research, Section B: Beam Interactions with Materials and Atoms, 326 (2014) 251-255.
[43] I.J. Fritz, Elastic properties of UO2 at high pressure, Journal of Applied Physics, 47 (2008) 4353-4358.
[44] B. Michel, M. Welland, N. Ofori-Opoku, L. Vanbrutzel, K. Kulacsy, M.R. Tonks, P.-G. Vincent, F. Ribeiro, A. Jelea, G. Pastore, D.A. Anderson, J.-m. Gatt, R. Madec, J.-P. Crocombette, State of the art of fuel micro-mechanical modelling: From atomic scale to engineering laws in fuel performance codes, Journal of Nuclear Materials, 572 (2022) 154034.
[45] M. Bertolus, M. Freyss, B. Dorado, G. Martin, K. Hoang, S. Maillard, R. Skorek, P. Garcia, C. Valot, A. Chartier, L. Van Brutzel, P. Fossati, R.W. Grimes, D.C. Parfitt, C.L. Bishop, S.T. Murphy, M.J.D. Rushton, D. Staicu, E. Yakub, S. Nichenko, M. Krack, F. Devynck, R. Ngayam-Happy, K. Govers, C.S. Deo, R.K. Behera, Linking atomic and mesoscopic scales for the modelling of the transport properties of uranium dioxide under irradiation, Journal of Nuclear Materials, 462 (2015) 475-495.
[46] W.F. Cureton, R.I. Palomares, J. Walters, C.L. Tracy, C.-H. Chen, R.C. Ewing, G. Baldinozzi, J. Lian, C. Trautmann, M. Lang, Grain size effects on irradiated CeO2, ThO2, and UO2, Acta Materialia, 160 (2018) 47-56.